Spectrochimica Acta Part A: Molecular and Biomolecular Spectroscopy 302 (2023) 123020

Contents lists available at ScienceDirect

Spectrochimica Acta Part A: Molecular and Biomolecular Spectroscopy

journal homepage: www.journals.elsevier.com/spectrochimica-acta-part-a-molecular-and-biomolecular-spectroscopy

WMS-based near-infrared on-chip acetylene sensor using polymeric SU8 Archimedean spiral waveguide with Euler S-bend

Huan Zhao [a], Chuantao Zheng [a,*], Mingquan Pi [a], Lei Liang [b], Fang Song [a], Kaiyuan Zheng [d], Yu Zhang [a], Yiding Wang [a], Frank K. Tittel [c]

[a] State Key Laboratory of Integrated Optoelectronics, College of Electronic Science and Engineering, Jilin University, Changchun 130012, China
[b] State Key Laboratory of Luminescence and Applications, Changchun Institute of Optics Fine Mechanics and Physics, Chinese Academy of Sciences, Changchun 130033, China
[c] Department of Electrical and Computer Engineering, Rice University, 6100 Main Street, Houston, TX 77005, USA
[d] Department of Electrical Engineering and Photonics Research Institute, The Hong Kong Polytechnic University, Hong Kong, China

HIGHLIGHTS

- On-chip C_2H_2 measurement using polymeric SU8 waveguide was demonstrated.
- Euler-S bend was adopted to reduce sensor size by more than a half.
- C_2H_2 measurement was performed using wavelength modulation spectroscopy (WMS).
- The SU8 spiral waveguide provides a compact, cost-effective way for gas sensing.

GRAPHICAL ABSTRACT

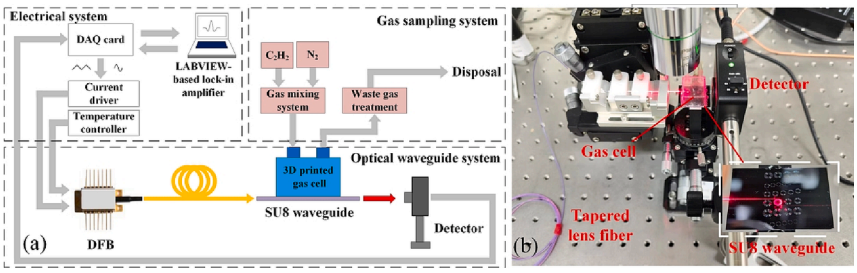

ARTICLE INFO

Keywords:
Gas sensor
SU8 waveguide
Euler S-bend
Wavelength modulation spectroscopy
Acetylene detection

ABSTRACT

SU8 is a cost-effective polymer material that is highly suitable for large-scale fabrication of waveguides. However, it has not been employed for on-chip gas measurement utilizing infrared absorption spectroscopy. In this study, we propose a near-infrared on-chip acetylene (C_2H_2) sensor using SU8 polymer spiral waveguides for the first time to our knowledge. The performance of the sensor based on wavelength modulation spectroscopy (WMS) was experimentally validated. By incorporating the proposed Euler-S bend and Archimedean spiral SU8 waveguide, we achieved a reduction in the sensor's size by over fifty percent. Leveraging the WMS technique, we evaluated the C_2H_2 sensing performance at 1532.83 nm for SU8 waveguides of lengths 7.4 cm and 13 cm. The limit of detection (LoD) values were 2197.1 ppm (parts per million) and 425.5 ppm, respectively, with an averaging time of 0.2 s. Furthermore, the experimentally obtained optical power confinement factor (PCF) closely approximated the simulated value, with a value of 0.0172 compared to the simulated value of 0.016. The waveguide loss is measured to be 3 dB/cm. The rise time and fall time were approximately 2.05 s and 3.27 s, respectively. This study concludes that the SU8 waveguide exhibits significant potential for high-performance on-chip gas sensing in the near-infrared wavelength range.

* Correspondence author.
E-mail address: zhengchuantao@jlu.edu.cn (C. Zheng).

https://doi.org/10.1016/j.saa.2023.123020
Received 7 May 2023; Received in revised form 4 June 2023; Accepted 14 June 2023
Available online 19 June 2023

1. Introduction

The rapid progress in industrial production has significantly stimulated the advancement of gas sensor research [1–3]. Real-time, portable and cost-effective measurement of specific gases are crucial for waste gas treatment, energy mining, flammable and explosive gas monitoring [4,5]. Various types of gas sensing systems have been developed using discrete optical elements and techniques such as tunable laser absorption spectroscopy (TLAS) [6], cavity enhanced absorption spectroscopy (CEAS) [7], photoacoustic spectroscopy (PAS) [8], and photothermal spectroscopy (PTS) [9], among others. However, the size of these sensors poses limitations on their portability. Consequently, there has been an increasing demand for the development of real-time, portable, and miniaturized gas sensor systems [10,11].

To achieve miniaturization, electrochemical sensing has gained widespread use owing to its high resolution, good repeatability, and cost-effectiveness [12,13]. However, electrochemical sensors do possess certain limitations, including a short lifespan, limited selectivity, and susceptibility to temperature variations. Alongside electrochemical sensing, gas sensors utilizing optical waveguides have also garnered significant attention in recent years [14,15]. Optical waveguide gas sensing techniques mainly consist of refractive index sensing and optical absorption sensing [16,17]. The concentration level of the analyte can be extracted from the change of the effective refractive index, which affects the output light frequency or phase from the waveguide, by monitoring the refractive index of the analyte as the waveguide cladding material varies with the concentration [18]. However, due to the limited change range of gas refractive index, the detection sensitivity is low, and the selectivity for analytes is poor. In contrast to refractive index sensing, waveguide sensors based on optical absorption spectroscopy provide greater selectivity since each analyte has a unique absorption spectrum [19]. Concentration can be determined by detecting light attenuation when the evanescent waveguide mode field with a specific wavelength passes through the analyte.

Due to the limited interaction length between the optical waveguide and the gas analyte, as well as the mode transmission loss in the waveguide, the research on optical waveguide gas sensors has primarily focused on increasing the effective absorption optical path length. In 2011, Chen et al. first used infrared absorption spectroscopy to gas sensing on optical waveguides. They proposed an on-chip sensor based on a silicon photonic crystal slot waveguide for detecting CH_4 concentration in the near-infrared, successfully demonstrating its capability to detect 100 parts-per-million (ppm) CH_4 [11]. Photonic crystal waveguides offer slow light effect, and the electric field in the slot waveguide is significantly enhanced, leading to a substantially increased effective absorption optical path length compared to the physical waveguide length. Subsequently, a series of on-chip gas sensing studies were conducted using photonic crystal waveguides [15,20]. Additionally, gas sensing based on conventional waveguides has also been reported. In 2017, Green et al. employed tunable diode laser absorption spectroscopy (TDLAS) to assess CH_4 sensing performance in a 10 cm-long silicon waveguide at 1650 nm, achieving a LoD at sub-ppm levels [21]. Suspended waveguide structures have also been utilized to enhance the overlap between light and analytes. In 2021, Jagerska et al. measured the concentration of acetylene (C_2H_2) using a Ta_2O_5 suspended ridge waveguide at 2.566 μm, obtaining a LoD as low as 7 ppm [22]. Furthermore, on-chip gas measurements using microcavity and surface-functionalized materials have been employed to enhance sensing performance [23,24].

Depending on optical waveband, various waveguide materials have been employed for optical absorption spectroscopic gas sensing. Silicon waveguides have been utilized for detecting methane (CH_4) concentration in the near-infrared range, achieving a sub 100 ppm LoD [21]. Chalcogenide (ChG) glasses have typically been used in the mid-infrared range due to their low absorption loss [25,26]. In order to achieve single-mode transmission, the waveguide's cross-sectional size needs to be small, resulting in mode mismatch with the coupling optical fiber. Consequently, a mode spot converter or grating coupler is required, which involves expensive techniques such as electron beam lithography (EBL) or deep ultraviolet lithography (DUV) [23,27]. In addition to these materials, polymers also serve as potential platforms for gas sensing, including SU8 (EPONSU-8, Microchem), which exhibits high transmittance within the 0.4–5 μm wavelength range [28]. SU8 is a negative photoresist based on EPONSU-8 epoxy resin, commonly used in microstructure processing. For SU8 waveguides, the fabrication process is straightforward and does not require etching or film deposition. The size of a single-mode SU8 waveguide falls within the micron range, and it can be achieved using conventional UV lithography. Additionally, the coupling mismatch with the optical fiber's end face is small, and the loss of SU8 waveguides is relatively low [29].

Presently, SU8 has been employed in on-chip gas sensing, including its usage as a light guide medium. The material's sensitive coating reacts with the gas, leading to changes in absorbance, and consequently detecting gas concentration through light intensity attenuation [30,31]. Furthermore, SU8 is employed as a support layer in gas sensors based on Micro Electromechanical Systems (MEMS) [32,33]. Here, we propose a spiral SU8 waveguide sensor design with C_2H_2 detection using different sensing lengths, instead of the more commonly used silicon and ChG waveguides. The polymeric SU8 waveguides are applied to gas sensing based on infrared absorption for the first time to our knowledge. Further, in the design of spiral waveguides, we utilized Euler S-bend, which effectively reduces the waveguide dimension size by more than half. C_2H_2 measurement with WMS resulted in a LoD down to the level of hundreds of ppm, which suggests that SU8 is promising for high sensitivity on-chip gas sensing.

2. SU8 spiral waveguide structure and gas sensing theory

Fig. 1(a) shows the proposed SU8 spiral waveguide structure. The materials of the core layer and lower cladding layer are SU8 and SiO_2, respectively. The refractive index of SU8 and SiO_2 at 1532.83 nm are 1.573 and 1.46, respectively. At the center of the spiral waveguide, there is a S-bend waveguide composed of two Euler bends. There are input/output straight waveguides at both sides, which are connected to the S-bend waveguide through Archimedes spiral waveguides [34,35]. The curvature of the Archimedes spiral changes gradually, while each pair of neighboring circular waveguides is equally spaced.

The basic theory of a waveguide gas sensor obeys the Lambert-Beer Law. Since only the evanescent field interacts with the gas analyte when the light transmits in the waveguide, it is necessary to modify the Lambert-Beer Law as follows [36]

$$I_1 = I_0 \exp(-\Gamma \alpha_{gas} cL - \alpha_{int} L) \tag{1}$$

where I_1 and I_0 are output and input light intensity of the waveguide, c is the gas concentration, α_{gas} is the absorption coefficient, α_{int} is the intrinsic loss of the SU8 waveguide, and L is the waveguide length of the sensing area. Γ is defined as the power confinement factor (PCF), which can be expressed as

$$\Gamma = \frac{n_g \iint_{cl} \varepsilon |E|^2 dxdy}{Re\{n_{cl}\} \int \int_{-\infty}^{\infty} \varepsilon |E|^2 dxdy} \tag{2}$$

Here, n_g is the group refractive index, n_{cl} is the refractive index of gas, ε is the permittivity, and E is the electric field. PCF represents the fraction of light power confined within the evanescent field, which corresponds to the portion of light that interacts with the gas sample. PCF incorporates the impact of waveguide dispersion, as represented by the group refractive index. The product between PCF and the length of the sensing waveguide (L) provides the equivalent absorption optical path length in free space. The intensity of light absorption is related to four parameters: the power confinement factor, gas absorption coefficient, waveguide loss, and gas concentration. In our experiment, we

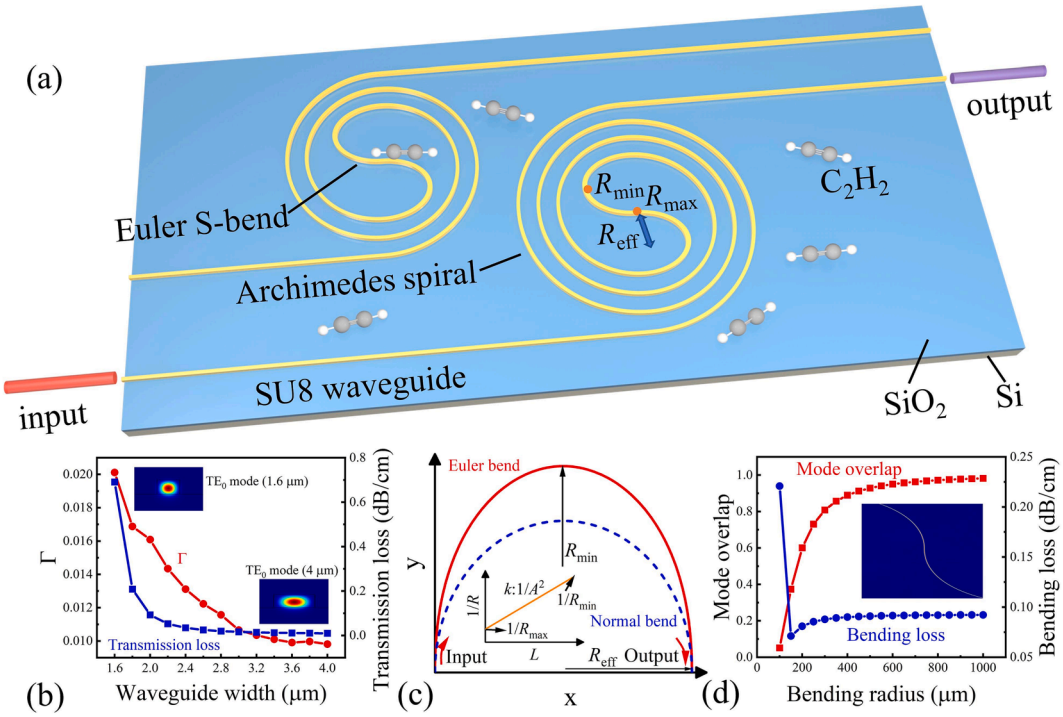

Fig. 1. (a) Schematic of the SU8 spiral waveguide sensor, which is composed of two Euler S-bend waveguides, an Archimedes spiral waveguide and two straight waveguides. (b) Relation curve of transmission loss and Γ versus waveguide width. The insets show the TE mode field distribution with waveguide width of 1.6 μm and 4 μm, respectively. (c) Schematic configuration of Euler bend (red line) and normal bend (blue line). The inset shows the relationship between the bending radius R of the Euler bend and the curve length L. (d) The mode overlap factor at the Euler S-bend junction with different maximum radius R_{max} and bending loss with different minimum radius R_{min}. The inset shows the light transmission in Euler S-bend. (For interpretation of the references to colour in this figure legend, the reader is referred to the web version of this article.)

utilized SU8-2002 with a coating thickness of 1.5 μm. Hence, the parameters that can be optimized are waveguide width and length. Fig. 1 (b) illustrates the curves of transmission loss and the Γ of the TE mode under different waveguide widths, calculated using finite difference eigenmode (FDE). As the waveguide width increases, both the transmission loss and Γ decrease. The reduction in loss can be attributed to the smaller overlap between the mode and the waveguide's side wall. The decrease in Γ is a result of the increased waveguide width, which enhances the ability to confine the optical mode. To achieve a balance between waveguide loss and the power confinement factor, we set the waveguide width to 2 μm and Γ to 0.016.

In order to achieve greater chip sensing compactness, we have adopted Euler bends instead of the typical bends. Fig. 1(c) shows the schematic configuration of Euler bend (red line) and normal bend (blue line). The 180° Euler bend consists of two symmetric 90° Euler bends, which are determined by the maximum and the minimum bending radius (defined as R_{max} and R_{min}). The curvature of Euler bend changes linearly with the increase of curve length, which is defined as

$$\frac{d\theta}{dL} = \frac{1}{R} = \frac{L}{A^2} + \frac{1}{R_{max}} \tag{3}$$

where R is the bending radius, L is the waveguide length, A is a constant, which determines the rate of curvature change, as shown in the illustration in Fig. 1(a). The Euler bend curve can be expressed in Cartesian coordinates, as shown in Eq. (4) and Eq. (5)

$$x = A\int_0^{L/A} \sin\left(\frac{\theta^2}{2} + \frac{A\theta}{R_{max}}\right) d\theta \tag{4}$$

$$y = A\int_0^{L/A} \cos\left(\frac{\theta^2}{2} + \frac{A\theta}{R_{max}}\right) d\theta \tag{5}$$

To minimize mode mismatch at the junction of Euler bend waveguide (R_{max}), it is necessary to have a sufficiently large maximum bending radius. Simultaneously, R_{min} should be small enough to reduce sensor size and large enough to guarantee low-loss single-mode transmission. The width and thickness of the SU8 waveguide is 2 μm and 1.5 μm, respectively. Fig. 1(d) shows the calculated mode overlap factor at the Euler S-bend junction with different R_{max} and bending waveguide loss with different R_{min} using the FDE solver in MODE Solutions. As the bending radius increases, the overlap factor of the optical field mode at the two Euler bending junctions approaches 1. Due to device size limitations and fabrication errors, R_{max} is set to 700 μm, while R_{min} is set to 200 μm to reduce the bending loss of the spiral waveguide. The effective radius R_{eff} is approximately 260 μm. Adopting a normal bend would require a radius of at least 700 μm. For the 7.4 cm-long waveguide, the area of the curved waveguide is reduced from about ~ 9 mm^2 to 2.1 mm^2, and for the 13 cm-long waveguide, the area is reduced from ~ 13.3 mm^2 to 4.4 mm^2. The device becomes more compact by over 50% through the use of the Euler S-bend design that decreases the size of the spiral waveguide. The inset in Fig. 1(d) shows the TE mode field transmission in Euler S-bend waveguide.

3. Fabrication and measurement

3.1. SU8 spiral waveguide fabrication and transmission loss measurement

The fabrication process of SU8 waveguide is simple and cost-effective compared to traditional silicon-based waveguide processes. Initially, the silicon dioxide wafer's surface is cleaned using oxygen plasma. After that, SU8 is spin-coated, and photolithography and development are performed. Finally, a series of baking processes are necessary to complete the fabrication process of SU8 waveguide.

The fabricated SU8 spiral waveguides with different lengths are shown in Fig. 2(a), and compact design and layout allow multiple waveguide tests on the same chip. The cross-sectional scanning electron

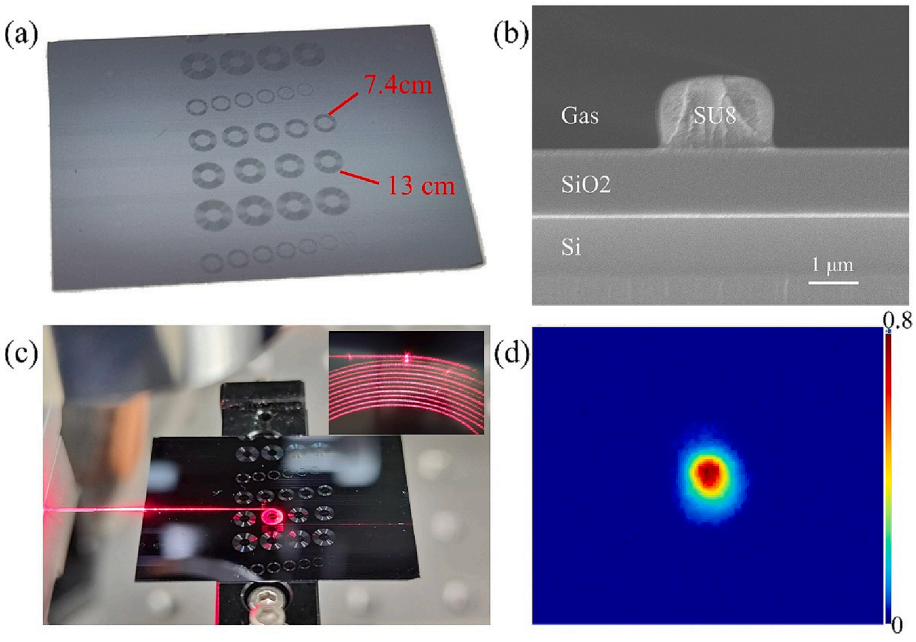

Fig. 2. (a) A photo of the fabricated SU8 spiral waveguides. (b) Cross-sectional SEM image of the SU-8 waveguide. (c) Microscopic photos with red light coupled into the spiral waveguide. The inset shows a detailed characterization of the spiral waveguides with red light propagation. (d) Waveguide output spot observed by a near-field infrared camera. (For interpretation of the references to colour in this figure legend, the reader is referred to the web version of this article.)

microscope (SEM) image of the fabricated SU8 waveguide is shown in Fig. 2(b). Fig. 2(c) displays the observation of red light transmission under a microscope using a tapered lens fiber to couple the light into the SU8 waveguide. Hence, red light can assist in aligning the optical fiber and waveguide during the test. To evaluate the light transmission performance of the waveguide in the near-infrared band, a 1532 nm distributed feedback (DFB) laser (DFB-1532-I-N-1-SM, Tengguang) is coupled into the SU8 waveguide through a tapered lens fiber, and the near-field infrared camera (CMOS 1203-IR, Cinogy) is used to monitor the waveguide's output. As depicted in Fig. 2 (d), the emission pattern exhibits an approximately Gaussian type, indicating excellent performance of SU8 waveguide in the near-infrared waveband.

To evaluate the transmission loss of the SU8 waveguide, a broadband light source (ASE-C/L-100-FA-B, Ltss) is used to couple a laser beam into the waveguide via a tapered lens fiber. The output of the waveguide is coupled with another lens fiber, which is linked to an optical fiber spectrometer (AQ6370D, Yokogawa) to measure the transmission loss. Two waveguides with lengths of 7.4 cm and 13 cm are tested, and the output spectra are shown in Fig. 3(a). The process involves subtracting the two spectra and dividing the difference in spectra by the difference in length to determine the waveguide loss, as demonstrated in Fig. 3(b). At 1532 nm, the loss of the SU8 waveguide is approximately 3 dB/cm. However, the loss measured is higher than expected due to the neglect of the actual roughness of the waveguide side walls during the simulation. Improving the fabrication process can help reduce the waveguide loss. Additionally, increasing the waveguide length can improve absorbance and achieve lower LoD within an acceptable range of the total transmission loss. Consequently, lengths of 7.4 cm and 13 cm were selected for testing.

3.2. Experimental setup and details for C_2H_2 sensing

The schematic diagram of on-chip C_2H_2 sensing system based on the fabricated SU8 spiral waveguide is shown in Fig. 4(a). A distributed feedback (DFB) laser operating at 1532 nm was employed to scan the absorption line of C_2H_2 positioned at 1532.83 nm by modifying the driving current. A three dimensional (3D) printed gas cell was bonded to the SU8 sensor chip. Through a tapered lens fiber, the light from the DFB laser was coupled into the SU8 waveguide, and the output light was spatially coupled to an InGaAs detector (PDA20CS2, Thorlabs), which converted the optical signal to an electrical signal. Through a LabVIEW-controlled data acquisition (DAQ) card, a triangular wave signal and high-frequency sine wave signal for driving the laser were generated and supplied to the laser driver (LDC210C, Thorlabs). The LabVIEW-based

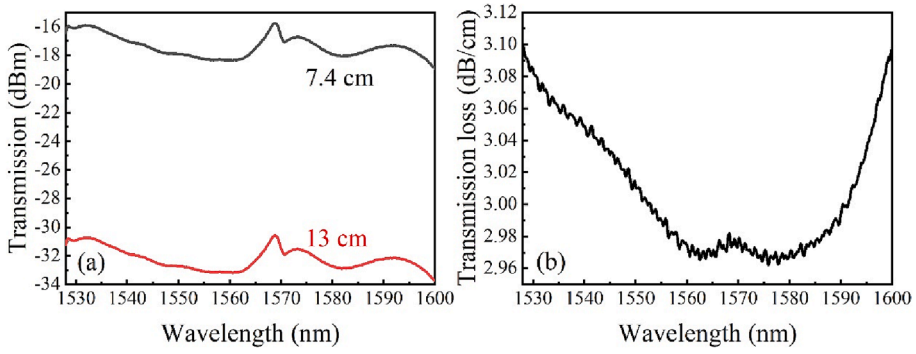

Fig. 3. (a) The measured output spectra of two waveguides with lengths of 7.4 cm and 13 cm when a tunable broadband laser beam is input into the waveguides. (b) Calculated SU8 waveguide loss.

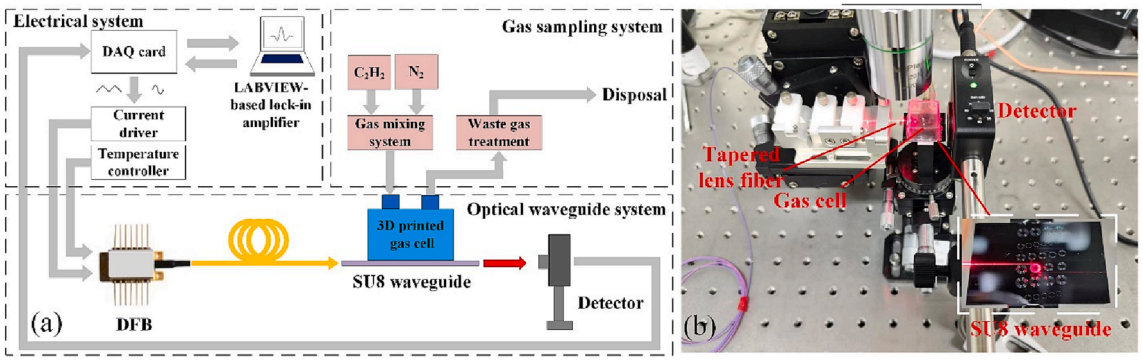

Fig. 4. (a) Schematic diagram of the on-chip C_2H_2 sensing system; (b) A photo of the optical waveguide sensor system. The inset shows the transmission of red light in the SU8 spiral waveguide. (For interpretation of the references to colour in this figure legend, the reader is referred to the web version of this article.)

signal processing program was used to deal with the absorption signal. Fig. 4(b) shows a photo of the optical waveguide system. The alignment of the waveguide output to the detector can be assisted by introducing red light into the waveguide, as shown in the inset.

In order to scan the absorption line of C_2H_2 at 6023.88 cm^{-1}, the operating temperature of the DFB laser was set to 32 ℃. The wavelength scan signal of the DFB laser has a start voltage of 0.4 V and an amplitude of 0.45 V, leading to a current range of 40 – 85 mA. The emission wavelength of the DFB laser can sweep from 6523.26 to 6524.49 cm^{-1}. The sampling rate of the DAQ card is 5 kHz, resulting in 2×10^4 data points in each scanning cycle. In order to obtain the gas absorbance at the same time, at the rising edge (with modulation) and falling edge (without modulation) of the scan signal, gas measurements were performed based on WMS and direct absorption spectroscopy (DAS), respectively.

3.3. Absorbance and power confinement factor

A gas dilution system (Environics, Series 4000) was used to mix acetylene (C_2H_2) and N_2, resulting in five prepared acetylene samples with concentration levels of 0%, 10%, 20%, 30%, and 40%. Two SU8 waveguides with lengths of 7.4 cm and 13 cm were selected for DAS and WMS measurements. The prepared gas samples were injected into the gas cell for 5 min at each concentration and the resulting absorption signal and absorbances were recorded using a LabVIEW-based signal processing program with a sampling period of 0.2 s. The measured absorbance of the 7.4 cm and 13 cm-long waveguides are shown in Fig. 5 (a) and Fig. 5(b).

The *PCF* can be obtained by analyzing the measured absorbance. When pure N_2 is injected into the gas cell, the relationship between the output and input light intensity is

$$I_1^{'} = I_0 \exp(-\alpha_{int} L) \tag{6}$$

Then the relationship between absorbance and PCF can be obtained by Eq. (1) and Eq. (6), as shown below

$$\text{Absorbance} = -\ln\left(I_1/I_1^{'}\right) = \Gamma \alpha_{gas} c L \tag{7}$$

For the 13 cm-long waveguide, the measured absorbance is 0.051 at 40% C_2H_2 concentration. According to the high-resolution transmission (HITRAN) database, the α_{gas} of C_2H_2 at 1532.83 nm is 0.57 cm^{-1}. Therefore, the measured PCF of the SU8 waveguide is 0.0172, which is close to the theoretical value of 0.016 calculated by simulation.

3.4. Modulation amplitude optimization and sensor calibration using WMS

Prior to WMS measurement, modulation amplitude should be optimized to enhance the second harmonic (2*f*) signal, and consequently, the signal-to-noise ratio (SNR). At a C_2H_2 concentration level of 30%, the measured 2*f* signal amplitude using the 7.4 cm and 13 cm-long waveguides was experimentally obtained under different modulation amplitudes, as shown in Fig. 6. The 2*f* signal amplitude becomes the maximum when the modulation amplitude is 0.12 V. As the laser current had reached its maximum limit, modulation amplitude could not be increased any further, prompting the experiment to use 0.12 V as the modulation amplitude.

During WMS measurement, a triangle wave scan signal and a high-frequency sine wave modulation signal at 5 kHz were combined at the rising edge. Each gas sample was measured for 5 min at different C_2H_2 concentration levels, with a sampling period of 0.2 s. Both the 2*f* signal waveform and amplitude were recorded. The 2*f* signal waveforms of the 7.4 cm and 13 cm-long waveguides at different concentration levels are shown in Fig. 7(a) and 7(b), respectively.

The recorded 2*f* signal amplitude was averaged at each concentration, and the relationship between the 2*f* signal amplitude and C_2H_2

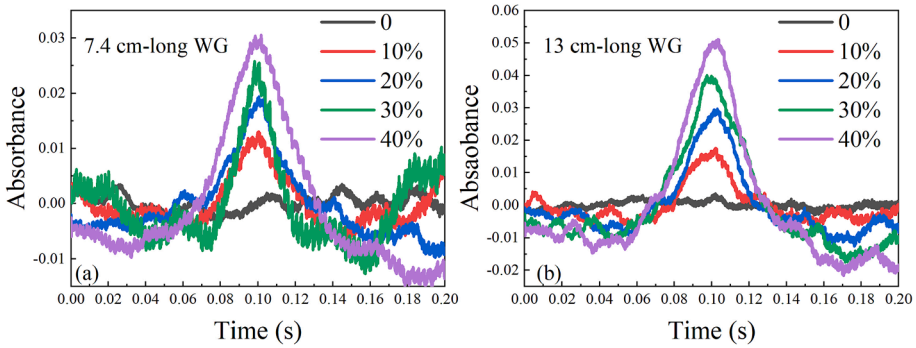

Fig. 5. The measured absorbance of the (a) 7.4 cm-long waveguide and (b) 13 cm-long waveguide under different C_2H_2 concentration levels of 0, 10%, 20%, 30% and 40%.

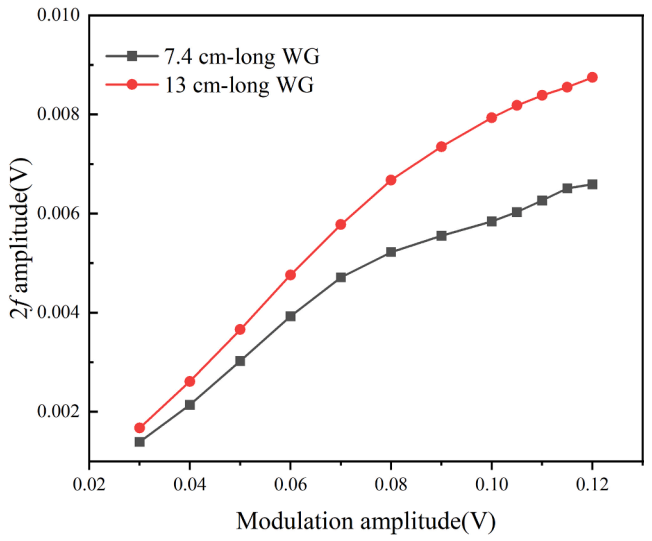

Fig. 6. The relationship between the measured 2*f* signal amplitude and modulation amplitude under 30% C_2H_2 concentration level for the 7.4 and 13 cm-long waveguide sensors.

concentration of the 7.4 cm- and 13 cm-long waveguides is shown in Fig. 7(c) and 7(d). The relation curve between the 2*f* signal amplitude (denoted by Max(2*f*), V) and the C_2H_2 concentration (*C*, ppm) are linearly fitted as

$$\mathrm{Max}(2f)_{7.4\mathrm{cm}} = 1.5878 \times 10^{-8} C + 0.00195 \quad (8)$$

$$\mathrm{Max}(2f)_{13\mathrm{cm}} = 2.49139 \times 10^{-8} C + 0.00153 \quad (9)$$

3.5. Stability

In order to evaluate the stability and noise level of the waveguide sensor, inject pure N_2 into the gas cell and record the 2*f* signal amplitude with a data sampling time of 0.2 s. Using Eq. (8) and Eq. (9) to convert the 2*f* signal amplitude into concentration. The time series of the measured C_2H_2 concentration levels versus observation time are shown in Fig. 8(a) and 8(b). Curves of the Allan deviation versus averaging time based on the measurement data in Fig. 8(a) and 8(b) are shown in Fig. 8 (c). The 1σ LoD (σ represents Allan deviation) of the 7.4 cm-long and 13 cm-long waveguides are 2197.1 ppm and 425.5 ppm at an averaging time of 0.2 s. The LoD of the 7.4 cm-long waveguide is 281.4 ppm at an optimum averaging time of 40.2 s, while the LoD of the 13 cm-long waveguide is 28.7 ppm at an optimum averaging time of 48.6 s.

From Fig. 5, it is evident that the ratio of absorbance for the 7.4 and 13 cm-long SU8 waveguides is approximately equal to the ratio of their lengths at different concentrations. However, it is noteworthy that the background noise for the 7.4 cm waveguide is higher compared to that of the 13 cm waveguide. The LoD determined by Allan deviation is influenced by both the absorbance and noise. Consequently, the difference in LoD is slightly larger than the disparity in waveguide length. It is speculated that the noise primarily originates from mechanical vibration of the optical fiber. To mitigate this issue, future work can focus on packaging and integrating the sensing waveguide with the optical fiber to minimize the effects of mechanical vibration noise.

3.6. Response time

To evaluate the response time of the waveguide sensor system, pure N_2, 20% C_2H_2 sample and pure N_2 was injected into the gas cell in turn. The 2*f* signal amplitude obtained using the 7.4 cm-long waveguide was recorded, and the C_2H_2 concentration variation was converted according to Eq. (8). The measurement results are shown in Fig. 9. The measured 10%–90% rise time and 90–10% fall time are ~ 2.05 s and ~ 3.27 s, respectively.

3.7. Performance comparison

This section compares the performance of the reported silicon photonic CH_4 sensor [21] with the SU8 spiral waveguide C_2H_2 sensor proposed in this paper, as shown in Table 1. With a concentration level of

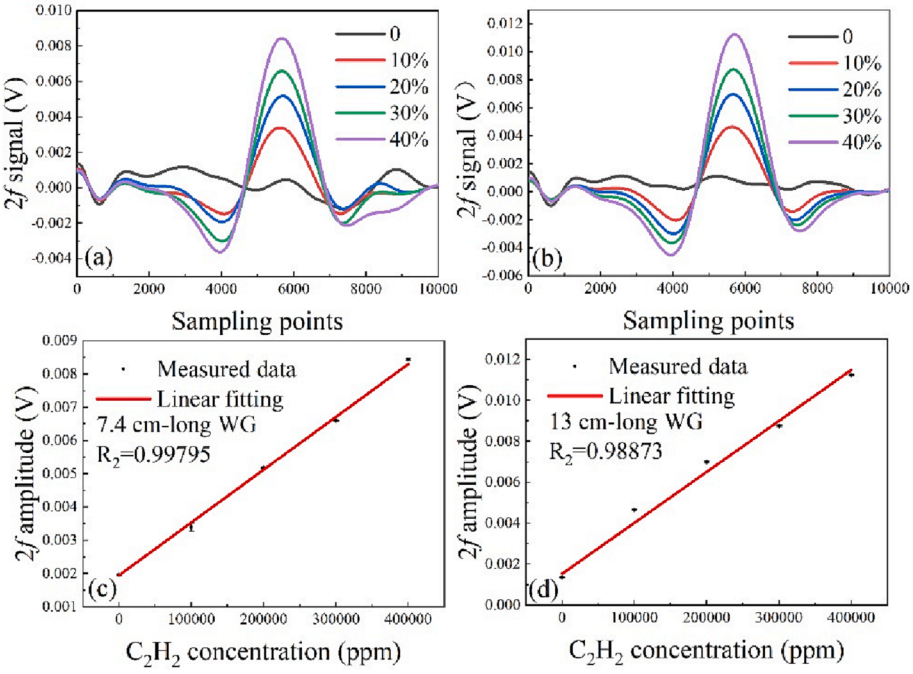

Fig. 7. The measured 2*f* signal under C_2H_2 concentration levels of 0, 10%, 20%, 30% and 40% for the (a) 7.4 cm-long and (b) 13 cm-long waveguides. The measured data dots and linear fitting curve of the 2*f* signal amplitude under C_2H_2 concentration levels of 0, 10%, 20%, 30% and 40% for the (c) 7.4 cm-long and (d) 13 cm-long waveguides.

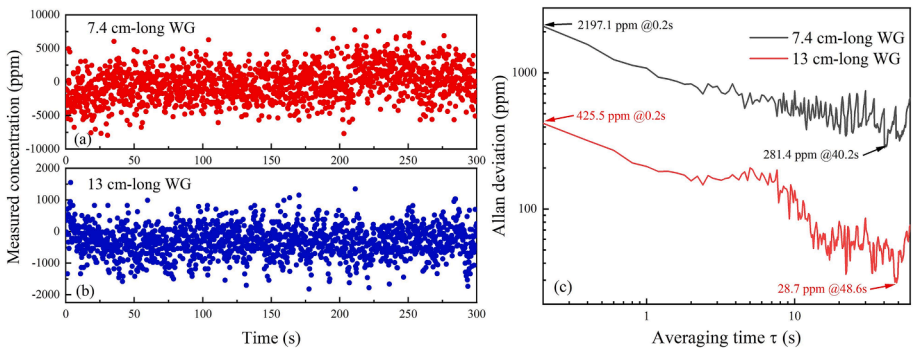

Fig. 8. The measured C_2H_2 concentration levels in N_2 environment using the (a) 7.4 cm-long and (b) 13 cm-long waveguides. (c) Allan deviation analysis based on the data shown in (a) and (b) for the two waveguide sensors.

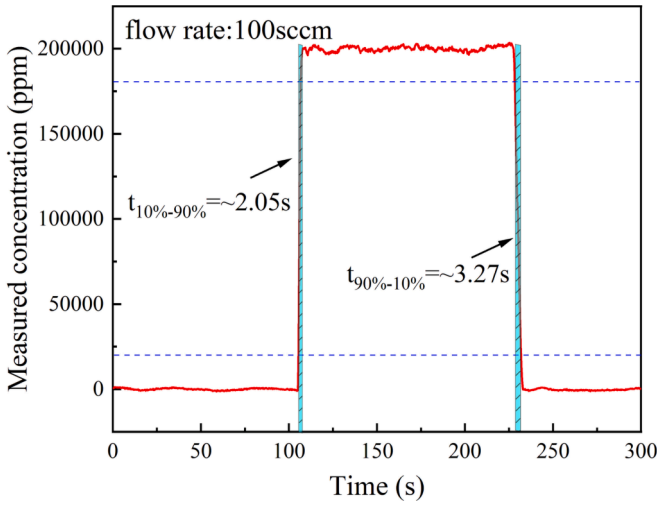

Fig. 9. Response time measurement by injecting C_2H_2 samples with concentration levels of 0 ppm (N_2), 20% and 0 ppm (N_2).

100%, the absorption coefficient of CH_4 at 1653.7 nm is 0.3 cm^{-1}, which is close to 0.57 cm^{-1} of C_2H_2 at 1532.8 nm.

The CH_4 sensor based on a silicon photonic spiral waveguide with a normal bend was evaluated using DAS technique. In terms of waveguide length, loss, absorption coefficient, both types of sensors are comparable. The PCF of the silicon waveguide is significantly greater than that of the SU8 waveguide by one order of magnitude. The relatively weak PCF of the SU8 waveguide is a limiting factor that affects its sensing performance. To improve the light-gas interaction, it becomes necessary to increase the waveguide length. However, the small refractive index difference between the SU8 material and cladding requires a larger bending radius, resulting in an increase in device size. In this paper, an Euler S-bend was utilized to reduce device size while achieving a waveguide length of more than 10 cm. Due to the use of WMS, the LoD of the SU8 waveguide can also reach the order of 100 ppm, which is at the same level as that of the silicon waveguide. Conventional ultraviolet lithography can fabricate the microns order wide SU8 single mode waveguide. The SU8 waveguide can be easily coupled with a tapered lens fiber without the necessity of mode spot converters or grating couplers, and red light coupling can achieve efficient alignment.

In comparison with the waveguides made from other materials, SU8 waveguides offer several advantages for gas sensing applications. Firstly, the fabrication process of SU8 waveguides is straightforward, cost-effective, and compatible with the commonly used substrate materials. Additionally, the wide transparency range of SU8 enables the use of red light for alignment during testing, which simplifies the measurement process. Moreover, due to the large cross-sectional size and minimal coupling mismatch with fiber mode field, SU8 waveguides have the potential for large-scale, low-cost waveguide-fiber packaging. However, it is worth noting that SU8 waveguides also have certain limitations, including a lower power limiting factor and relatively larger waveguide size.

To address the issue of the low power limiting factor, one potential solution is to fabricate a suspended waveguide, which can enhance the overlap between the evanescent field and the gas. Additionally, the SU8 waveguide exhibits low-loss transmission at wavelengths below 5 μm, making it suitable for mid-infrared gas sensing applications. Given the significant gas absorption in the mid-infrared band, it can compensate for the low PCF and allow for a reduction in the waveguide's length and size while maintaining effective gas interaction.

4. Conclusions

On-chip C_2H_2 measurement at the wavelength 1532.83 nm was realized using SU8 spiral waveguide DAS for the first time to our knowledge. The use of an Euler S-bend design significantly reduces the dimension size of the spiral waveguide by more than 50% compared to the normal bend structure, allowing for high integration of sensors on a single chip. Two SU8 waveguides of different lengths (7.4 cm and 13 cm) were utilized for C_2H_2 sensing based on WMS. At an averaging time of 0.2 s, the LoD for the two waveguide sensors are 2197.1 ppm and 425.5 ppm, respectively. The LoD can reach 281.4 and 28.7 ppm by increasing the averaging time to 40.2 s and 48.6 s, respectively. The measured PCF of the fabricated SU8 waveguide is 0.0172 with an optical loss of ~ 3 dB/cm. By further PCF optimization and reducing waveguide loss, a lower LoD can be expected. The SU8 spiral sensing waveguide offers a compact, cost-effective solution for high-performance on-chip gas sensing.

Table 1
Comparison between the reported silicon photonic CH_4 sensor and this sensor.

Refs.	Wavelength (μm)	Waveguide material and type	Technique	*L*(cm)	α_{int} (dB/cm)	PCF (%)	LoD (ppm)
[21]	1.654	Silicon normal spiral	DAS	10	2	25.4	100@1min
This paper	1.532	SU8 Euler S-bend spiral	WMS	7.4	3	1.72	2197@0.2 s
				13			425@48.6 s

CRediT authorship contribution statement

Huan Zhao: Conceptualization, Methodology, Software, Writing – original draft. **Chuantao Zheng:** Conceptualization, Methodology, Supervision, Writing – review & editing. **Mingquan Pi:** Conceptualization, Methodology, Software, Validation. **Lei Liang:** Methodology, Validation. **Fang Song:** Writing – original draft. **Kaiyuan Zheng:** Writing – original draft. **Yu Zhang:** Supervision. **Yiding Wang:** Writing – review & editing, Supervision. **Frank K. Tittel:** Writing – review & editing.

Declaration of Competing Interest

The authors declare that they have no known competing financial interests or personal relationships that could have appeared to influence the work reported in this paper.

Data availability

Data will be made available on request.

Acknowledgement

The authors would like to express their gratitude to the National Natural Science Foundation of China (Nos. 62175087, 62235016, 61960206004, 62105118), Science and Technology Development Program of Jilin Province, China (Nos. 20200401059GX, 20230201054GX), Science and Technology Research Project of Department of Education, Jilin Province, China (No. JJKH20211088KJ), Key R&D Program of Changchun (No. 21ZGN24), and Program for JLU Science and Technology Innovative Research Team (JLUSTIRT, 2021TD-39).

References

[1] J.S. Li, G. Durry, J. Cousin, L. Joly, B. Parvitte, V. Zeninari, Self-broadening coefficients and positions of acetylene around 1.533 μm studied by high-resolution diode laser absorption spectrometry, J. Quant. Spectrosc. Radiat. Transf. 111 (2010) 2332–2340.
[2] K.C. Utsav, E.F. Nasir, A. Farooq, A mid-infrared absorption diagnostic for acetylene detection, Appl. Phys. B-Lasers Opt. 120 (2015) 223–232.
[3] G.M. Ma, S.J. Zhao, J. Jiang, H.T. Song, C.R. Li, Y.T. Luo, H. Wu, Tracing Acetylene Dissolved in Transformer Oil by Tunable Diode Laser Absorption Spectrum, Sci. Rep. 7 (2017) 14961.
[4] K.Y. Zheng, C.T. Zheng, Q.X. He, D. Yao, L. Hu, Y. Zhang, Y.D. Wang, F.K. Tittel, Near-infrared acetylene sensor system using off-axis integrated-cavity output spectroscopy and two measurement schemes, Opt. Express 26 (2018) 26205–26216.
[5] T.N. Chen, F.X. Ma, Y. Zhao, Y.K. Zhao, L.J. Wan, K. Li, G.Q. Zhang, Portable ppb-level acetylene photoacoustic sensor for transformer on-field measurement, Optik 243 (2021), 167440.
[6] J.A. Silver, Frequency-modulation spectroscopy for trace species detection: theory and comparison among experimental methods, Appl. Optics 31 (1992) 707–717.
[7] M. Abe, K. Iwakuni, S. Okubo, H. Sasada, Design of cavity-enhanced absorption cell for reducing transit-time broadening, Opt. Lett. 39 (2014) 5277–5280.
[8] A.A. Kosterev, Y.A. Bakhirkin, R.F. Curl, F.K. Tittel, Quartz-enhanced photoacoustic spectroscopy, Opt. Lett. 27 (2002) 1902–1904.
[9] Y.M. Ma, C.T. Zheng, L. Hu, K.Y. Zheng, F. Song, Y. Zhang, Y.D. Wang, F.K. Tittel, High-robustness near-infrared methane sensor system using self-correlated heterodyne-based light-induced thermoelastic spectroscopy, Sens. Actuators, B 370 (2022), 132429.
[10] Y.Y. Qiao, J.F. Tao, J.F. Q, X.B. Hong, J. Wu, Sensitive and ultrasmall sample volume gas sensor based on a sealed slot waveguide, Appl. Opt. 58 (2019) 4708–4713.
[11] W.C. Lai, S. Chakravarty, X.L. Wang, C.Y. Lin, R.T. Chen, On-chip methane sensing by near-IR absorption signatures in a photonic crystal slot waveguide, Opt. Lett. 36 (2011) 984–986.
[12] Y.Z. Wang, H.X. Qiu, S.Q. Hu, J.H. Xu, A novel methyl parathion electrochemical sensor based on acetylene black-chitosan composite film modified electrode, Sens. Actuator B-Chem. 147 (2010) 587–592.
[13] N. Tarnaekong, C. Liewhiran, A. Wisitsoraat, S. Phanichphant, Acetylene sensor based on Pt/ZnO thick films as prepared by flame spray pyrolysis, Sens. Actuator B-Chem. 152 (2011) 155–161.
[14] M.Q. Pi, C.T. Zheng, R. Bi, H. Zhao, L. Liang, Y. Zhang, Y.D. Wang, F.K. Tittel, Design of a mid-infrared suspended chalcogenide/silica-on-silicon slot-waveguide spectroscopic gas sensor with enhanced light-gas interaction effect, Sens. Actuator B-Chem. 297 (2019), 126732.
[15] K.M. Yoo, J. Midkiff, A. Rostamian, C.J. Chung, H. Dalir, R.T. Chen, InGaAs Membrane Waveguide: A Promising Platform for Monolithic Integrated Mid-Infrared Optical Gas Sensor, ACS Sens 5 (2020) 861–869.
[16] R.A. Soref, F. De Leonardis, V.M.N. Passaro, On-Chip Detection of Trace Gases Using Photonic Matched Filters, J. Lightwave Technol. 37 (2019) 1388–1395.
[17] C. Ranacher, C. Consani, U. Hedenig, T. Grille, V. Lavchiev, B. Jakoby, A Photonic Silicon Waveguide Gas Sensor Using Evanescent-Wave Absorption, IEEE Sensors (2016).
[18] R.S. El Shamy, M.A. Swillam, D.A. Khalil, Mid Infrared Integrated MZI Gas Sensor Using Suspended Silicon Waveguide, J. Lightwave Technol. 37 (2019) 4394–4400.
[19] M.A. Butt, S.A. Degtyarev, S.N. Khonina, N.L. Kazanskiy, An evanescent field absorption gas sensor at mid-IR 3.39 mu m wavelength, J Mod. Opt. 64 (2017) 1892–1897.
[20] C. Blin, Z. Han, H.A. Girard, P. Bergonzo, P. Boucaud, M. El Kurdi, S. Saada, S. Sauvage, X. Checoury, Surface-sensitive diamond photonic crystals for high-performance gas detection, Opt. Lett. 41 (2016) 4360–4363.
[21] L. Tombez, E.J. Zhang, J.S. Orcutt, S. Kamlapurkar, W.M.J. Green, Methane absorption spectroscopy on a silicon photonic chip, Optica 4 (2017) 1322–1325.
[22] M. Vlk, A. Datta, A. Rostamian, S. Alberti, H.D. Yallew, V. Mittal, G.S. Murugan, J. Jagerska, Extraordinary evanescent field confinement waveguide sensor for mid-infrared trace gas spectroscopy, Light-Sci. Appl. 10 (2021) 26.
[23] A. Nitkowski, L. Chen, M. Lipson, Cavity-enhanced on-chip absorption spectroscopy using microring resonators, Opt. Express 16 (2008) 11930–11936.
[24] M.Q. Pi, C.T. Zheng, J.L. Ji, H. Zhao, Z.H. Peng, J.M. Lang, L. Liang, Y. Zhang, Y. D. Wang, F.K. Tittel, Surface-Enhanced Infrared Absorption Spectroscopic Chalcogenide Waveguide Sensor Using a Silver Island Film, ACS Appl. Mater. Interfaces 13 (2021) 32555–32563.
[25] P. Su, Z. Han, D. Kita, P. Becla, H. Lin, S. Deckoff-Jones, K. Richardson, L. C. Kimerling, J. Hu, A. Agarwal, Monolithic on-chip mid-IR methane gas sensor with waveguide-integrated detector, Appl. Phys. Lett. 114 (2019), 051103.
[26] M.Q. Pi, Y.J. Huang, H. Zhao, Z.H. Peng, J.M. Lang, J.L. Ji, L. Teng, F. Song, L. Liang, Y. Zhang, C.T. Zheng, Y.D. Wang, F.K. Tittel, Theoretical and experimental investigation of on-chip mid-infrared chalcogenide waveguide CH_4 sensor based on wavelength modulation spectroscopy, Sens. Actuator B-Chem. 362 (2022), 131782.
[27] Z.M. Ding, Z.X. Liu, L. Wu, Z.Y. Zhang, Material contact sensor with 3D coupled waveguides, Opt. Express. 29 (2021) 39055–39064.
[28] S. Chakravarty, J. Midkiff, A. Rostamian, J. Guo, R. T. Chen, Monolithic Integration of Quantum Cascade Laser, Quantum Cascade Detector and Slotted Photonic Crystal Waveguide for Absorbance Sensing from lambda = 3-15 μm, 2018 Conference on Lasers and Electro-Optics (CLEO) (2018).
[29] K. Gut, Z. Opilski, Spectropolarimetric analyses of optical single mode SU8 waveguide layers, Bull. Pol. Acad. Sci.-Tech. Sci. 63 (2015) 349–352.
[30] A. Airoudj, B. Beche, D. Debarnot, E. Gaviot, F. Poncin-Epaillard, Integrated SU-8 photonic gas sensors based on PANI polymer devices: Comparison between metrological parameters, Opt. Commun. 282 (2009) 3839–3845.
[31] A. Airoudj, D. Debarnot, B. Beche, F. Poncin-Epaillard, Development of an optical ammonia sensor based on polyaniline/epoxy resin (SU-8) composite, TALANTA 77 (2009) 1590–1596.
[32] T. Iwata, W.P.C. Soo, K. Matsuda, K. Takahashi, M. Ishida, K. Sawada, Design, fabrication, and characterization of bridge-type micro-hotplates with an SU-8 supporting layer for a smart gas sensing system, J. Micromech. Microeng. 27 (2017), 024003.
[33] J. Zacharias, K.H. Nikhita, V. Seena, Novel Polymer MEMS Capacitive Hydrogen sensor with Palladium Ring on Membrane-Mass Architecture, 2020 5th IEEE International Conference on Emerging Electronics (ICEE) (2020).
[34] S.A. Hong, L. Zhang, Y. Wang, M. Zhang, Y.W. Xie, D.X. Dai, Ultralow-loss compact silicon photonic waveguide spirals and delay lines, Photon. Res. 10 (2022) 1–7.
[35] X.H. Jiang, H. Wu, D.X. Dai, Low-loss and low-crosstalk multimode waveguide bend on silicon, Opt. Express. 26 (2018) 17680–17689.
[36] S. Schilt, L. Thevenaz, P. Robert, Wavelength modulation spectroscopy: combined frequency and intensity laser modulation, Appl. Opt. 42 (2003) 6728–6738.